In vivo photoacoustic potassium imaging of the tumor microenvironment

JOEL W. Y. TAN,[1,5] ⓘ JEFF FOLZ,[2,3,5] RAOUL KOPELMAN,[1,2,3,6] AND XUEDING WANG[1,4,7]

[1]*Department of Biomedical Engineering, University of Michigan, Ann Arbor, Michigan 48109, USA*
[2]*Biophysics Program, University of Michigan, Ann Arbor, Michigan 48109, USA*
[3]*Department of Chemistry, University of Michigan, Ann Arbor, Michigan 48109, USA*
[4]*Department of Radiology, University of Michigan Medical School, Ann Arbor, Michigan 48109, USA*
[5]*These authors contributed equally to this work.*
[6]*kopelman@umich.edu*
[7]*xdwang@umich.edu*

Abstract: The accumulation of potassium (K^+) in the tumor microenvironment (TME) has been recently shown to inhibit immune cell efficacy, and thus immunotherapy. Despite the abundance of K^+ in the body, few ways exist to measure it *in vivo*. To address this technology gap, we combine an optical K^+ nanosensor with photoacoustic (PA) imaging. Using multi-wavelength deconvolution, we are able to quantitatively evaluate the TME K^+ concentration *in vivo*, and its distribution. Significantly elevated K^+ levels were found in the TME, with an average concentration of approximately 29 mM, compared to 19 mM found in muscle. These PA measurements were confirmed by extraction of the tumor interstitial fluid and subsequent measurement via inductively coupled plasma mass spectrometry.

1. Introduction

Potassium (K^+) is the most abundant cation in the body [1]. The evolution of live cells started by keeping Na^+ out of and K^+ inside the cell [2,3]. Steep gradients exist in its distribution as intracellular K^+ concentrations are typically greater than 100 mM [1,4], while extracellular K^+ concentrations are approximately 5 mM [1]. It has long been known that the tumor microenvironment (TME) can have suppressive effects on T cells [5]. However, this suppression was only recently attributed to disruptions in the K^+ concentration [6]. Notably, necrotic cell death in the nutrient-starved core of tumors leads to the release of vast quantities of intracellular K^+. The release of this K^+ induces local *hyperkalemia* in the TME with a reported 5-10 fold increase in K^+ concentration [6]. In two seminal studies, Eil and colleagues determined that elevated K^+ suppresses T cell effector function and prevents immune cells from maturing [6,7].

Despite the importance of K^+ in the body, there exist only a few ways to measure K^+ concentrations *in vivo*. Magnetic resonance imaging (MRI) has been used in the past to measure *in vivo* K^+ concentrations [8–10]. However, the ^{39}K MRI imaging is an expensive technique, and is limited by availability and especially by poor resolution (voxel size of ~1 mL) [8]. Few commercially available potassium-sensitive dyes exist (PBFI, Asante-Green series), and of these none are excitable in either the near- or far-infrared. Visible wavelength dyes for fluorescence imaging are ill-suited for *in vivo* experiments due to the severe scattering of light in biological tissue. Miniaturized electrodes, the gold standard in ion measurement, are inherently invasive and unable to capture finely resolved spatial and temporal ion distribution images. It is of note that, in the previously mentioned immunological studies, K^+ was measured by centrifuging *ex vivo* tumors to collect tumor interstitial fluid [6,11], which was then measured via electrode, thus losing any spatiotemporal resolution.

To generate structural images that contain the chemical information in biological samples, we recently developed *photoacoustic chemical imaging* (PACI). PACI benefits on one hand from the good sensitivity of the optical detection techniques and on the other hand from the lower tissue scattering and thus excellent penetration and spatial resolution of ultrasound imaging [12,13]. PACI utilizes exogenous contrast agents, typically nanosensors, whose optical absorption properties change in response to some analyte of interest. The advantages of PACI have already allowed the monitoring of lithium treatments for bipolar disorder [14], measuring of tissue oxygenation using a lifetime-based approach [15–19], and measuring of tumor and gastrointestinal pH [20,21].

In this study, we extend PACI through the use of an ionophore-based optical K^+ nanosensor. While we have previously developed a K^+ sensor for PACI, it had a cross-sensitivity with pH due to its reliance on a pH dye as part of its sensing mechanism [22]. Hence, its accuracy would be affected by the acidic tumor microenvironment. As such, we adopted a pH-insensitive K^+ sensor for *in vivo* PACI measurements of K^+. Invented by Eric Bakker's group, this optode formulation utilizes positively charged, solvatochromic dyes which are pushed from the hydrophobic interior of the nanoparticle to its hydrophilic surface as potassium is chelated [23]. The transition between the interior and exterior of the nanoparticle forces a change in the dye's optical absorption spectrum which can be measured by PA imaging. The solvatochromic dye based K^+-sensing nanoparticle (SDKNP) is directly injected into subcutaneous tumors in mice, where its signal is deconvoluted from that of blood. This method could be extended to measuring other ions, such as Na^+ and Cl^- [24–26]. Specifically, here we demonstrate its utility by documenting *in vivo* the high overall concentration of K^+ in tumor tissue compared to that in healthy muscle, and quantitatively verifying PACI results using inductively coupled plasma mass spectrometry measurements on the interstitial fluid harvested from each tumor.

2. Methods

2.1. Materials

Millipore water was used for all syntheses and buffer preparations. Chemicals purchased from Sigma-Aldrich (St. Louis, Mississippi, USA) include Pluronic F-127, valinomycin, dioctyl sebacate, sodium tetrakis[3,5-bis(trifluoromethyl)phenyl]borate, potassium chloride, sodium chloride, calcium chloride dihydrate, magnesium chloride, 3-(N-morpholino)propanesulfonic acid, acetonitrile, acetic anhydride, 1-iodooctadecane, 2-methylbenzothiazole, (dimethylamino)cinnamaldehyde, sodium iodide, and methanol.

2.2. SD2 synthesis

Synthesis of SD2 was first reported by Eric Bakker's group, and few changes were made to the original protocol [23]. Briefly, 1.5 g 2-methylbenzothiazole and 3.8 g 1-iodooctadecane were dissolved and refluxed in acetonitrile for 24 hours. The solution was removed from heat and allowed to solidify. The crude product was precipitated in diethyl ether, collected, and washed several times in diethyl ether. 265 mg of this product, along with 122 mg (dimethylamino)cinnamaldehyde, was then dissolved in acetic anhydride and refluxed for 20 minutes. The reaction solution was then poured into a warm solution of 10 mM sodium iodide (in Millipore water). The dark purple precipitate was washed several times with water, dried, and collected.

2.3. Nanoparticle synthesis

The protocol for the synthesis of the SDKNP was developed by Eric Bakker's group [23]. To generate a concentrated solution of nanoparticles, the following protocol was used. 0.2 mg SD2 (synthesized in house, see above), 0.9 mg sodium tetrakis[3,5-bis(trifluoromethyl)phenyl]borate, 1.2 mg valinomycin, 5 mg Pluronic F-127, and 8.75 μL (8 mg) dioctyl sebacate were dissolved

in 3 mL of methanol. The methanol cocktail was then injected into 30 mL of Millipore water under vigorous stirring. The surface of the methanol-water mixture was blasted with nitrogen gas for 1 hour to remove the methanol. The nanoparticle solution was concentrated to the desired concentration using an Amicon Ultra-15 centrifuge filter (100k Da).

2.4. Mass spectrometry – solvatochromic dye characterization

Electrospray ionization mass spectrometry was performed by the University of Michigan's Mass Spectrometry Core.

### 2.5. DLS and zeta-potential

Dynamic light scattering and zeta-potential measurements were performed at a nanosensor concentration of 1 mg/mL using a Beckman Coulter analyzer.

2.6. MTT

HeLa cells (ATCC authenticated) were cultured in Dulbecco's Modified Eagle Media with 10% fetal bovine serum and 1% penicillin/streptomycin. 100,000 cells were plated on a 24 well plate and allowed to grow over night in 1 mL of growth media. SDKNPs were incubated for various times at a concentration of 1 mg/mL. Following incubation, 500 μL of incubation media was replaced with 500 μL of MTT solution (5 mg/mL in PBS) and incubated for 4 hours. Once finished, all media was removed from the wells and replaced with 1 mL of DMSO. This solution was then incubated for 1 hour at which point the solution was removed and its absorption spectrum measured in a UV-Vis spectrophotometer. Absorption peaks at 590 nm were compared, and all samples were repeated 4 times.

2.7. PA and UV calibration

For the UV calibration, K^+ calibration samples of 0, 1, 5, 10, 20, 30, 50, 70, 100, and 150 mM K^+ with 1 mg/mL of SDKNP were prepared. Samples were prepared in pH 7.4 MOPS-buffered saline solution containing physiologically relevant concentrations of interfering cations: sodium (150 mM), magnesium (1 mM), and calcium (2.6 mM). The absorption spectrum for each sample was obtained for a range of 400-800 nm using a Shimadzu 1600 UV-Vis Spectrophotometer (Shimadzu, Kyoto, Japan). For the PA calibration, K^+ calibration samples of 0, 1, 5, 10, 20, 30, 40, 50, 70, 100, and 150 mM K^+ with 10 mg/mL of SDKNP were prepared. 75 μL of each sample was added into a transparent PVC tubing. The tube samples were submerged in water for acoustic coupling. The tube samples were then imaged using a PA imaging system consisting of a tunable pulsed laser (Continuum, Santa Clara, CA, USA) and a 128-element ultrasound probe with frequency range of 7 to 15 MHz (CL15-7, Philips, Andover, MA, USA). The tunable pulsed laser pumped by the third harmonic of an Nd:YAG laser (Continuum, Santa Clara, CA, USA) has a pulse duration of 5 ns, a firing frequency of 10 Hz, and is capable of achieving wavelength tuning in the range of 410-680 nm and 710-2500 nm. The ultrasound probe was then connected to a commercially available research ultrasound platform (Vantage 256, Verasonics, Kirkland, WA, USA) for data acquisition. The resolution of our imaging system was previously measured to have a 226 μm lateral and 166 μm axial resolution at a depth of 6 mm [20]. The general PA imaging setup is shown in Fig. 1. The PA signal was obtained for 6 wavelengths of 545, 560, 576, 584, 605, and 625 nm. Each PA signal was averaged 20 times, with a total of 4 replicates performed for each sample. A simple light fluence correction was performed where the PA signal was normalized to the average energy measured for each wavelength using a power meter (Newport, Irvine, CA, USA).
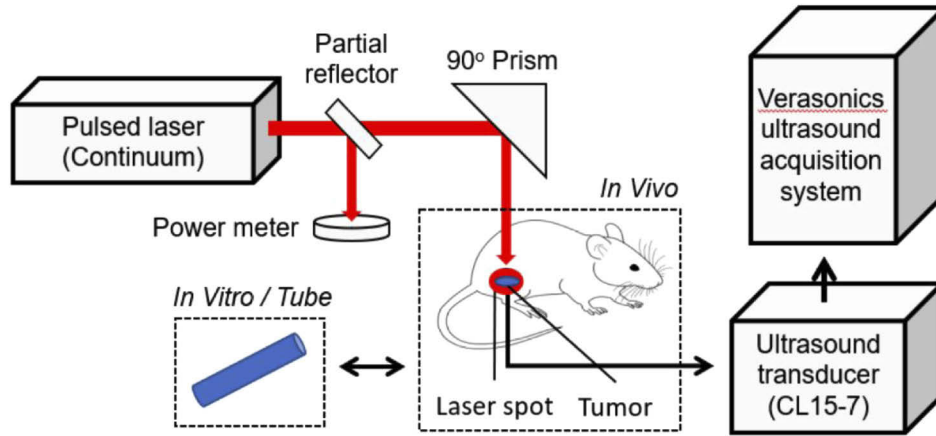
Fig. 1. General PA setup for *in vitro* and *in vivo* imaging. For acoustic coupling, *in vitro* tube experiments were conducted in water, while *in vivo* mice experiments were conducted using ultrasound gel. A partial reflector (glass slide) was used to reflect part (<20%) of the laser beam energy to the power meter for energy monitoring. The PA signal was acquired using an ultrasound transducer (CL15-7) connected to a research ultrasound acquisition system (Vantage 256, Verasonics, Kirkland, WA, USA).

2.8. PA multi-wavelength unmixing

An identical setup to the PA calibration experiment was performed. K^+ samples of 2, 5, 20, 40, 50, and 150 mM were prepared in the presence of 1% blood v/v and 10 mg/mL of SDKNP as well as a blank sample which only contained saline solution. PA imaging was conducted for 6 wavelengths of 545, 560, 576, 584, 605, and 625 nm. The wavelengths were chosen based on the isosbestic points and maximal difference in the extinction coefficients of SDKNP and hemoglobin. Multi-wavelength unmixing was performed according to the following steps. Firstly, at each wavelength, the PA signal can be modelled as shown in Eq. (1):

$$PA_\lambda = k([SDKNP]\varepsilon_{SDKNP}(\lambda, [K^+]) + [HbO_2]\varepsilon_{HbO_2}(\lambda) + [Hb]\varepsilon_{Hb}(\lambda)) \qquad (1)$$

where λ is the wavelength in nm, [SDKNP] is the SDKNP concentration, [HbO$_2$] is the oxyhemoglobin concentration, [Hb] is the deoxyhemoglobin concentration, [K$^+$] is the K$^+$ concentration, ε is the extinction coefficient, and k is a constant associated with multiple parameters such as light fluence, the Grüneisen parameter of the sample, and the sensitivity of the imaging system. It should be noted that ε_{SDKNP} is dependent on both λ and the K$^+$ concentration.

The extinction coefficients of Hb and HbO$_2$ for each λ are known values, while the extinction coefficient of SDKNP can be measured at each λ and for a range of K$^+$ values. Here, we measured the value of ε_{SDKNP} for K$^+$ values of 0, 1, 5, 10, 20, 30, 40, 50, 60, 70, 80, 90, 100, 125, 150, and 200 mM using a UV-VIS spectrophotometer. This left only 4 unknowns in the above equation, specifically [SDKNP], [HbO$_2$], [Hb], and [K$^+$]. Using simple linear algebra, the 4 unknowns can be solved by making at least 4 separate measurements at different wavelengths, similar to that performed by other groups [27,28]. Here, we used 6 wavelengths to solve the linear equations for increased accuracy, as it is widely known that additional measurements can help to improve the accuracy of the unmixed results [29–31]. Each set (6 wavelengths) of PA images are normalized to the maximum PA intensity within the imaging window of the entire set of PA images. The linear equations are then solved pixel-wise using a numerical approach by sweeping through positive discrete values of the 4 unknowns and calculating the minimum normalized mean absolute error. The errors from the 6 wavelengths measured are summed up, and the values

for the 4 unknowns that gives the lowest total error based on Eq. (1) is the deconvoluted signal. A notable limitation to this technique is that the estimation of the [K$^+$] is based on measurements of the extinction coefficient of the SDKNP at discrete K$^+$ values, meaning that the values of the measured K$^+$ are always limited to those discrete K$^+$ values. An alternative to this is to model the $\varepsilon_{\text{SDKNP}}$ response to K$^+$ by using an equation-based approach. This approach, while allowing for continuous K$^+$ estimates, has its own drawbacks in that no simple equation model can perfectly capture the $\varepsilon_{\text{SDKNP}}$ response to K$^+$, meaning that approximations will have to be made, reducing the accuracy of the measurements.

2.9.　In vivo PACI of K$^+$

Animal care was provided by the Unit for Laboratory Animal Medicine (ULAM), and all procedures on live animals were performed in accordance with institutional guidelines and approved by the Institutional Animal Care and Use Committee (IACUC) at the University of Michigan. A total of 6 mice were used in the *in vivo* imaging experiment. To generate the subcutaneous tumors, approximately 1×10^6 9L glioma cells (ATCC, Manassas, VA, USA) in 0.1 mL of RPMI 1640 (Gibco, Waltham, MA, USA) was subcutaneously injected into the right flank of 5-week old nude mice (Envigo, Huntingdon, Cambridgeshire, UK). The tumors were allowed to grow until a size of approximately 1 cm in diameter. 0.05 mL of 10 mg/mL SDKNP was then locally injected into the tumor, followed by PA imaging immediately after the injection. This was repeated with the thigh muscle on the opposite flank, where 0.05 mL of 10 mg/mL SDKNP was locally injected in the thigh muscle, followed by PA imaging immediately after the injection. All PA imaging was conducted for the same 6 wavelengths of 545, 560, 576, 584, 605, and 625 nm, with a total of 80 averages per image. A simple light fluence correction was performed where the PA signal was normalized to the average energy measured for each wavelength using the power meter. Multi-wavelength unmixing was conducted according to the same protocol as previously mentioned with the exception that only K$^+$ values between 0-125 mM were analyzed. This range was chosen to reflect the expected biological range of the extracellular tumor K$^+$.

　After the imaging, the mice were euthanized, and the tumor harvested. An adaptation of the protocol performed by Eil *et al.* was conducted to collect the extracellular fluid from the tumor. Briefly, the tumor was first flushed with saline to remove surface blood and blotted gently with Kimwipe (Kimberly-Clark, Irving, TX, USA) to dry. The tumor then was placed in a SpinX centrifuge tube filter (Corning, New York, NY, USA) and centrifuged at increasing speeds of 1000, 2000, 4000, and 8000 RPM for 10 minutes each [11]. Approximately 4-10 µL of extracellular fluid was collected per tumor. The extracellular fluid was then sent for inductively coupled plasma mass spectrometry.

2.10.　Inductively coupled plasma mass spectrometry (ICP-MS)

Tumor interstitial fluid was diluted with Millipore water by a factor of 5000 prior to measurement with a Perkin-Elmer Nexion 2000 ICP-MS (Perkin-Elmer, Waltham, MA, USA). The machine was calibrated using standards prepared at 50, 100, 250, 500, and 750 PPB K$^+$ using potassium chloride as a source for K$^+$ ions.

2.11.　Statistical analysis

All statistical analysis was performed using MATLAB 2016a (MathWorks, Natick, MA, USA). Where relevant, the data are expressed as the mean +/- standard deviation. Significant differences were determined using two-tailed two sample t-tests (*ttest2* function).

3.   Results

To test the capabilities of the SDKNP for PACI of K^+, we first compared the response of the SDKNP to K^+ using both PACI and UV-Vis spectrophotometry. Figure 2(a) shows the absorption spectra obtained for SDKNP at various K^+ levels. The largest absorption change occurred at 605 nm for the changing K^+ concentrations, with a small opposite trend at around 545 nm. The isosbestic point of the SDKNP is at approximately 560 nm. Making use of these wavelength ranges, the PA and UV-Vis calibration ratios were plotted in Figs. 2(b)–2(f). These calibration ratios show the changes in the PA and the UV-Vis signals with respect to the isosbestic point for increasing concentrations of K^+. As the PA signal of a molecule is directly proportional to its absorption, the PA calibration is expected to match that of the UV-Vis calibration. To show the good agreement between the PA and UV-Vis measurements, the ratios are co-plotted in Figs. 2(b)–2(f) to show the similarity between the ratios measured by both modalities. These ratios generally showed a signal decrease with increasing K^+ concentration, with exception of the 545 nm/560 nm ratio. The SDKNP is most sensitive between 0-50 mM K^+, an ideal range for the expected *in vivo* tumor K^+ concentration. Based on these results, we used the UV-Vis spectrophotometer measurements for later calibrations, as they generally provided measurements with very low noise levels.
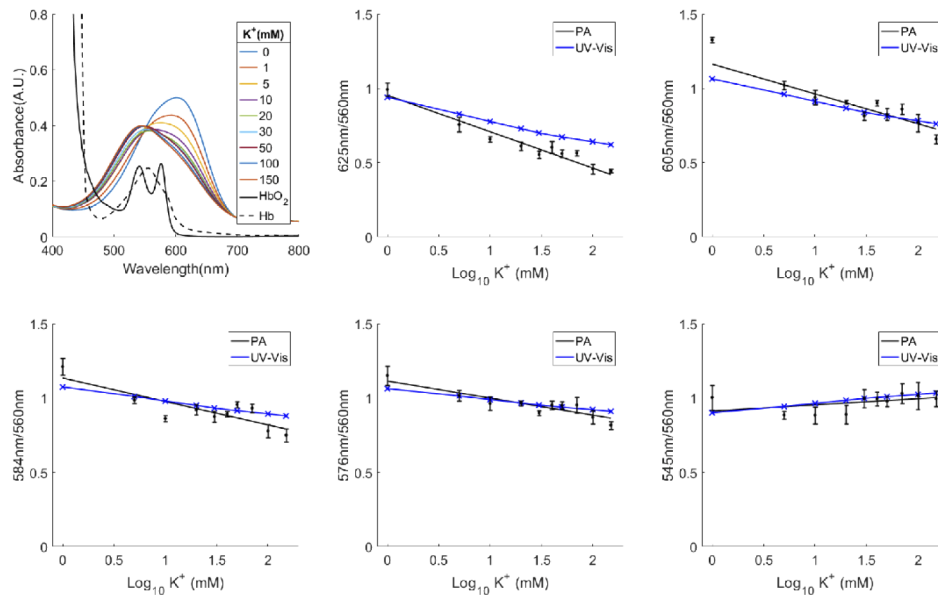
Fig. 2. Absorption spectra and PA K^+ calibrations compared to UV-Vis K^+ calibrations. (a) Absorption spectra of SDKNP for various K+ concentrations, oxyhemoglobin (HbO_2), and deoxyhemoglobin (Hb). PA and UV-Vis ratio measurements for (b) 625 nm/560 nm, (c) 605 nm/560 nm, (d) 584 nm/560 nm, (e) 576 nm/560 nm, and (f) 545 nm/560 nm. There is excellent agreement between the PA and UV-Vis calibrations.

Next, we analyzed the capability of separating the SDKNP signal from the expected *in vivo* endogenous chromophores of deoxyhemoglobin (Hb) and oxyhemoglobin (HbO_2). While other chromophores such as melanin and water are also present in biological tissue, Hb and HbO_2 are expected to be the major PA signal contributors within the 545-625 nm wavelength range in the tumor. Using a similar setup as the calibration experiment, multi-wavelength unmixing was performed for various K^+ samples in the presence of 1% blood v/v. This volume of blood was used as it is close to the estimated blood volume fraction in a tumor tissue (for breast cancer)

[32]. As mentioned in the Methods, the SDKNP concentration in each tube was consistently held at 10 mg/mL. Using a 6-wavelength unmixing technique, the concentrations of K^+, SDKNP, Hb, and HbO_2 were identified with the results shown in Fig. 3. The Hb and HbO_2 concentrations were then combined, as the oxygenation of the sample was not controlled and the total hemoglobin (THb) concentration was expected to serve as a more precise measurement. Within the SDKNP's sensitivity range of 0-50 mM, the unmixed measurements of K^+ concentration showed good accuracy levels (+/- 5 mM), with exception of the 20 mM sample. Outside this range, the measurement accuracy drops rapidly, although qualitative increases can be observed, as is shown by the significantly lower PACI estimate of 76 mM for the 150 mM K^+ sample. There is also some noticeable bleed through of the SDKNP and blood signals at higher K^+ concentrations (e.g. when [K +] was at 40 mM, 50 mM and 150 mM). This is most likely due to the absorption spectra of the SDKNP being more similar to blood at higher K^+ concentrations, especially that of deoxyhemoglobin [Fig. 2(a)]. It should be noted that this does not affect the K^+ measurement significantly, as most of the error is localized in the [SDKNP] and [THb] measurements. Finally, the blank sample showed almost no detectable signal throughout, as expected.
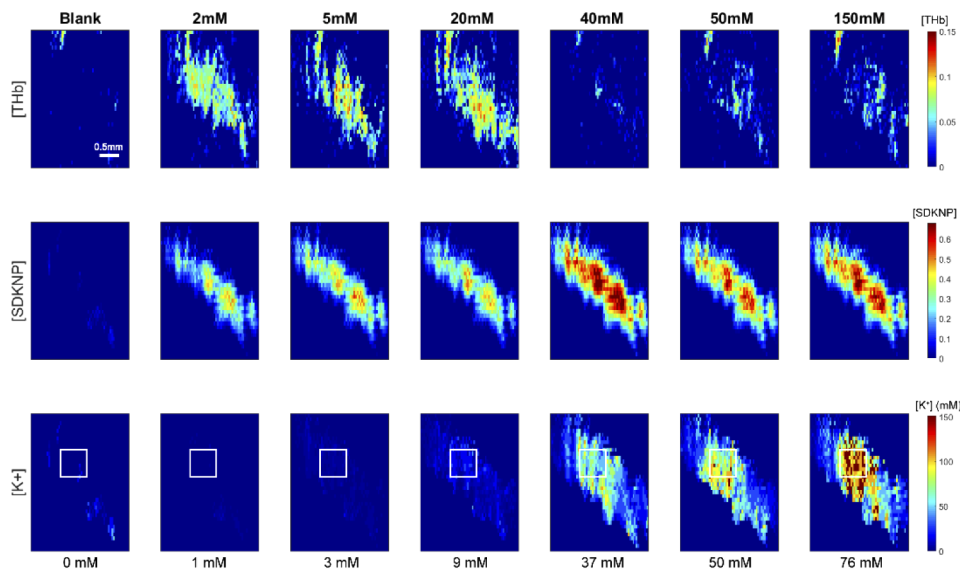
Fig. 3. PA multi-wavelength unmixing for SDKNP samples in a tube for determining total hemoglobin concentration ([THb]), SDKNP concentration ([SDKNP]), and K^+ concentration ([K^+]). All samples contain a constant 10 mg/mL SDKNP and 1% blood v/v at the specified K^+ concentrations, with exception of "Blank", which only contains saline solution. Sample values of K^+ are provided at the top of the figure, while the measured values obtained via deconvolution are given at the bottom of the figure. Measured values pertain to the average K^+ in the region of interest outlined by the white box.

After verifying the ability to measure the K^+ signal *in vitro* in the presence of blood, we then tested the ability to perform *in vivo* measurements of K^+ in a subcutaneous tumor mouse model. We locally injected 0.05 mL of 10 mg/mL SDKNP into the tumor and the thigh muscle of the mice before conducting PACI at the 6 wavelengths. Figure 4(a) shows an example of the map of oxygen saturation, SDKNP concentration, and K^+ concentration in the tumor and the muscle as measured by PA multi-wavelength unmixing for an individual mouse. Figure 4(b) shows the average hemoglobin oxygen saturation across all mice (n=6). While there is a slight decrease in the average tumor hemoglobin oxygen saturation compared to the muscle (47.5% compared to 52.3%), it was not statistically significant in this study. Figure 4(c) shows the average SDKNP

concentration across all mice, where there was no significant difference detected between the tumor and the muscle (0.024 vs 0.024 A.U.). As equal concentrations of SDKNP were injected into the tumor and the muscle, this result was expected. Figure 4(d) shows the average K^+ concentration between the tumor and the muscle, where the tumor K^+ was significantly higher than the muscle K^+ concentration. We observe an average K^+ concentration of 29 mM (range of 22-49 mM) in the TME, as expected from the predicted 5-10 fold increase report by Eil *et al*. [6]. In the muscle samples, we see an average concentration of 19 mM (range of 14-24 mM), which is higher than naively expected.
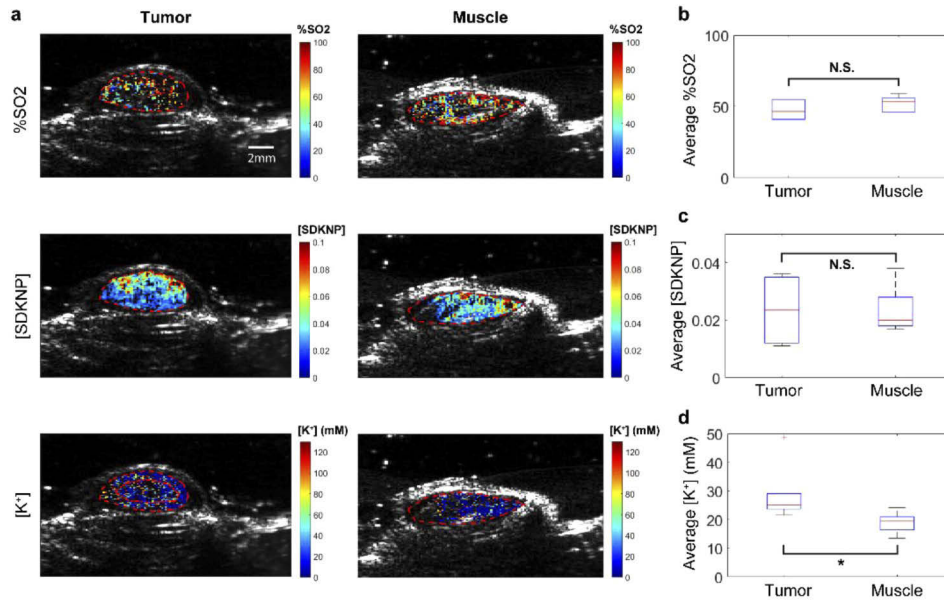

Fig. 4. *In vivo* PA imaging with overlaid ultrasound images of subcutaneous tumors and thigh muscles (control) in nude mice. (a) Multi-wavelength unmixing performed to identify the hemoglobin oxygenation saturation (%SO2), SDKNP concentration ([SDKNP]), and K^+ concentration ([K^+]). With exception of [K^+], images do not show 0 concentration values for better image clarity. Additionally, [K^+] concentrations are only shown where [SDKNP] are also present. The average value across all mice (n=6) in the tumor and the muscle for (b) %SO2, (c) [SDKNP], and (d) [K^+], as determined by multi-wavelength unmixing. 'N.S.' indicates no significance, '*' indicates p < 0.05.

To validate the accuracy of the K^+ measurements *in vivo*, we then measured the average K^+ concentration within the tumor via a method involving centrifugation to extract the interstitial fluid of the tumor, followed by ICP-MS to measure the K^+ concentration of the extracted fluid. The centrifugation method was used by Eil *et al*. to measure the K^+ concentration of the tumor [6]. The results of the ICP measurements are compared to the PACI measurements in Fig. 5. Figure 5(a) shows the average K^+ concentration measured by PACI vs ICP for each of the individual mouse tumors. Figure 5(b) shows a box plot of the distribution of average K^+ concentration measurements for PA imaging and ICP. Here, the mean value of the K^+ concentration measured using PACI was 29 mM (range of 22-49 mM), identical to the ICP-MS value of 29 mM (range of 15-48 mM). Figure 5(c) shows the correlation between the average K^+ concentration measurements made by PACI as compared to the ICP measurements. Generally, there was good agreement between the two K^+ concentration measurements, with an r^2 value of 0.70, based on a y = x linear regression fit. Based on the ICP measurement, we determined that

the average *in vivo* PACI K$^+$ concentration measurement error was 5 mM, while the maximum error was 11 mM.
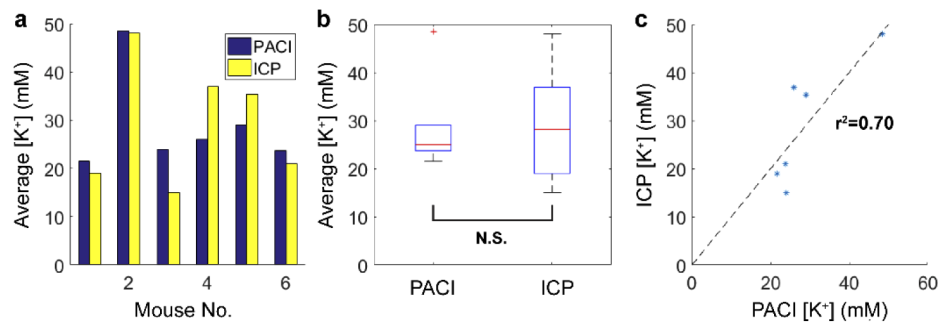
Fig. 5. Average [K$^+$] measurement in the tumor from PACI vs ICP. Average [K$^+$] in the tumor for (a) individual mouse measurements, and (b) across all mouse samples (n=6). 'N.S.' indicates no significance. (c) Correlation analysis between the ICP and the PACI measurements.

To further analyze the capability of our PACI technology for detecting spatial information within the tumor, we analyzed the K$^+$ distribution within the tumor core and the periphery. As it has been reported that the necrotic core was the cause of the elevated K$^+$ concentration in the tumor, we wanted to identify if there was a difference in the K$^+$ concentration within the tumor core (where the necrotic cores are expected), as compared to the peripheral regions of the tumor. Based on this, we would expect to see a higher K$^+$ concentration in the tumor core as opposed to the periphery. The results of our analysis are shown in Fig. 6, where an example of the determined regions of interest is shown in Fig. 6(a). The cores were demarcated by taking a region of approximately 40% of the entire demarcated tumor, centered around the estimated geometric center of the tumor. An approximately equal width (as allowed by the tumor shape) around the tumor core was then demarcated as the tumor periphery that comprised of the remaining 60% of the tumor. Here, we noted that there was an increase in the measured K$^+$ concentration in the tumor core for almost all the tumors [Fig. 6(b)], although this increase was small (an average of 3 mM or 10% higher). These observations suggest that elevated K$^+$ within tumors may not be uniform, and that this spatial difference can potentially be detected via PACI.
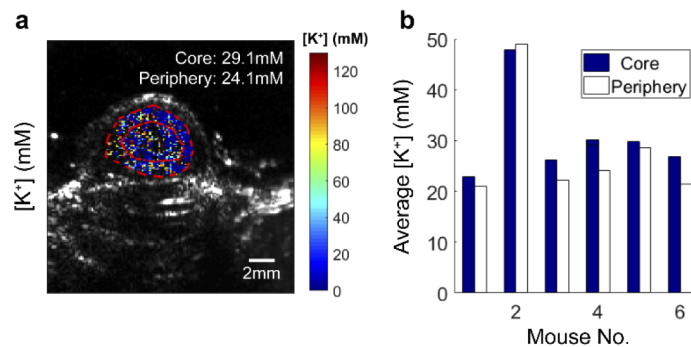
Fig. 6. Further analysis of the measured K$^+$ within the tumor core vs the tumor periphery. (a) An overlaid PA and ultrasound image showing the regions of interest of the core and the periphery, outlined in red. (b) Measured K$^+$ concentrations for each mouse for the tumor core and the tumor periphery.

4. Discussion

In this study, we demonstrate the ability of PACI to measure the K^+ concentration in a tumor *in vivo*, and show the elevated K^+ concentration in the tumor compared to the muscle tissue. These results were verified using ICP-MS with good correlation between the two independent measurement techniques (r^2=0.70). While Eil *et al.* have demonstrated that TME hyperkalemia induces elevated intracellular K^+, it remains unknown at what K^+ threshold this suppressive effect manifests itself. The ability to measure K^+ concentrations *in vivo* could provide an essential tool to the field of immunology, with studies no longer having to rely on *in vitro* measurements of K^+ at single time points with no spatial resolution. Additionally, an example of the spatial distribution of the TME hyperkalemia, as measured by our PACI technique, has been provided here. While the observed tumor K^+ heterogeneity was small, this may not be the case at a different time point of the tumor's development, especially at long times and for large tumors. Instead of the generalized tumor core vs periphery, future work can also be performed to compare necrotic regions of the tumor based on histological information and look at the measured *in vivo* K^+ concentrations with respect to those regions. PACI of K^+ is ideally suited for characterizing these physiological phenomena, allowing for quantitative and spatial measurements of K^+ in an *in vivo* mouse tumor, and potentially in a patient's tumor.

There are still improvements that can be made with the K^+ measurement. Regarding the discrepancies seen in Fig. 3, besides instrument calibration errors (UV-Vis spectrophotometer, ICP-MS), the PACI errors are mainly attributed to inaccuracies in the multi-wavelength unmixing technique, due to the wavelength-dependent light fluence attenuation in the sample, namely the "rainbow effect", and the wavelength-dependent laser energy output. While the latter is mostly corrected for by monitoring the laser energy through the partial reflector in the setup, the former is significantly more challenging to correct. A significant amount of research has been dedicated to this area, where methods to model the light fluence distribution in a tissue sample are being studied [33–35]. Without this wavelength-dependent light fluence correction, quantitative PA imaging is usually limited to surface/subcutaneous tumors. In a previous study, we have shown good accuracy within 6 mm depth from the tumor surface [20]. Additionally, there was some concern that the differences seen in the K^+ concentration in the tumor core and periphery might be due to fluence changes with depth. However, the fact that there was no difference in the K^+ distribution in the deeper and near-surface side of the tumor periphery suggests that this K^+ difference was not caused by depth-related changes. Besides light fluence modelling, increasing the number of wavelengths used in the imaging and multi-wavelength unmixing can also improve the accuracy of the measurements [29–31]. The latter method, however, has its own drawbacks in that the imaging time will be significantly increased, depending on the number of wavelengths desired.

Additionally, there are some concerns regarding the toxicity of the current formulation of the SDKNP. While not having significant toxicity within 2 hours, prolonged exposure does cause significant cell death in an MTT study (Fig. 11 in Appendix 3). This toxicity is largely attributable to the use of valinomycin as the K^+ ionophore and limited the study to intratumoral injections of the SDKNP. However, we first wanted a clear-cut demonstration of PACI of K^+, thus using this literature's most validated ionophore [23]. That being said, intratumoral injection does limit the applications of this current nanosensor to tumors that are both accessible for local injection and with a known location. In the future, adjustments can be made to the nanoparticle matrix to allow for substitution with a less toxic ionophore, such as BME-44 [36]. Notably, the Pluronic polymer is highly biocompatible and in wide medical use [37]. That being said, the strength of using these ionophore-based optical sensors is the relative ease at which sensors for other cations (like Na^+) and anions (like Cl^-) can be developed [36]. For example, substituting valinomycin for a sodium ionophore allows for the development of a PA sodium sensor with relative ease. Additional substitution of ionophores and plasticizers would allow for sensing multivalent cations, such as

magnesium, calcium, or transition metal ions, though non-trivial adjustments would be required, especially as the physiological concentrations of these species are much lower than that of K^+.

5. Conclusion

Despite its ubiquitous and abundant presence in the body, our ability to analyze K^+ concentration *in vivo* remains largely limited to the one-dimensional results gathered from electrodes. Here, we extended our previous work on PACI of tissue oxygenation and pH to include K^+. The effort utilized an exogenous contrast agent whose change in optical absorption spectrum allows for PA probing of the K^+ concentration. Our technique was first verified *in vitro* and then implemented *in vivo* for measuring the concentration and characterizing the spatial distribution of K^+ within the TME. We compared the here described PACI measurement results to those initially used to describe tumor hyperkalemia and found good agreement between them. In summary, this work represents the first *in vivo* PA measurement of K^+ and a robust expansion of PACI.

Appendix 1: Solvatochromic dye characterization

The solvatochromic dye utilized by the nanosensor is synthesized in house using a protocol developed by Eric Bakker's group [23]. We report here the mass spectrum of the final product in Fig. 7 (Bakker: 559.5; Ours: 559.4).
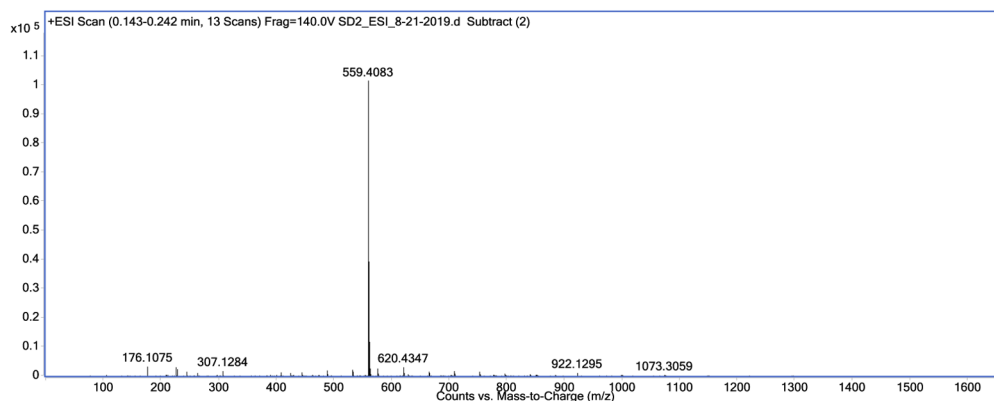

Fig. 7. Mass spectrum of the synthesized and purified dye using the protocol described in the methods section. Measurements were made using positive ion electrospray mass spectrometry and performed by the University of Michigan's Mass Spectrometry Core. The reported mass of the dye was 559.5 Da; we measured a mass of 559.4 Da.

### Appendix 2: Solvatochromic dye, potassium-sensing nanoparticle (SDKNP) characterization

SDKNP size was evaluated using both dynamic light scattering (Fig. 8) and transmission electron microscopy (Fig. 9). DLS measurements are seen in Fig. 8, where we observed an average nanosensor diameter of **90 nm** with a polydispersity index (PDI) of **0.107**. Zeta potential (ζ) measurements indicated that the SDKNP is highly stable, with a ζ of **-69.0 mV**.

TEM measurements of nanoparticle diameter yielded an average diameter of 45 nm. DLS values are often larger than those measured by TEM, and the discrepancies are attributed to variations in particle swelling as a result in changes of water content during sample preparation.

As the SDKNP's function depends on the ability of the solvatochromic dye heads to transition between phases, we wondered if protein adsorption to the nanoparticle's surface would inhibit this
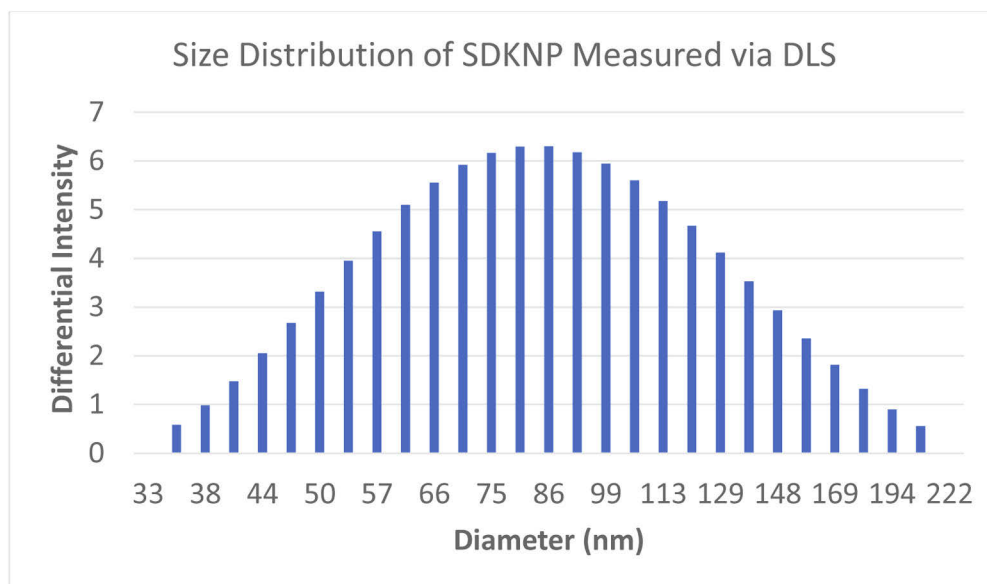
Fig. 8. Dynamic Light Scattering measurements of SDKNP diameter. The average nanosensor size is 90 nm, with a PDI of 0.107.
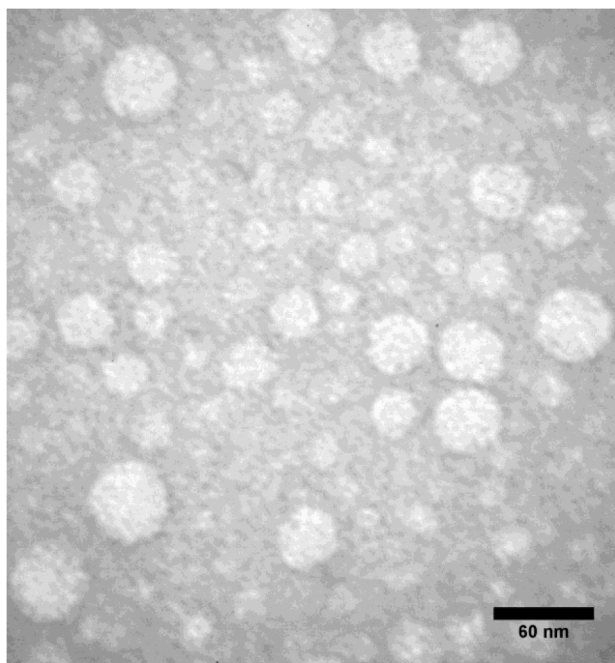
Fig. 9. TEM images of the SDKNP taken at 5 mg/mL in water. An average diameter of approximately 50 nm is observed.

phase transition, and therefore sensing. To test the effect of proteins in solution, we conducted two calibration curves of the SDKNP: one with 5 mg/mL human serum albumin (HSA) and the other without any albumin. Figure 10 shows that the albumin had little effect on the sensor's response. All calibrations were taken in MBS, containing the physiologically relevant concentrations of cations (150 mM Na, 1 mM Mg, and 2.6 mM Ca). Additionally, the presence of redox species in the TME is expected to have minimal effect on the sensor, as the ionophore, valinomycin, is exquisitely selective, and the sensing components are embedded in and protected by the Pluronic F-127 polymers.
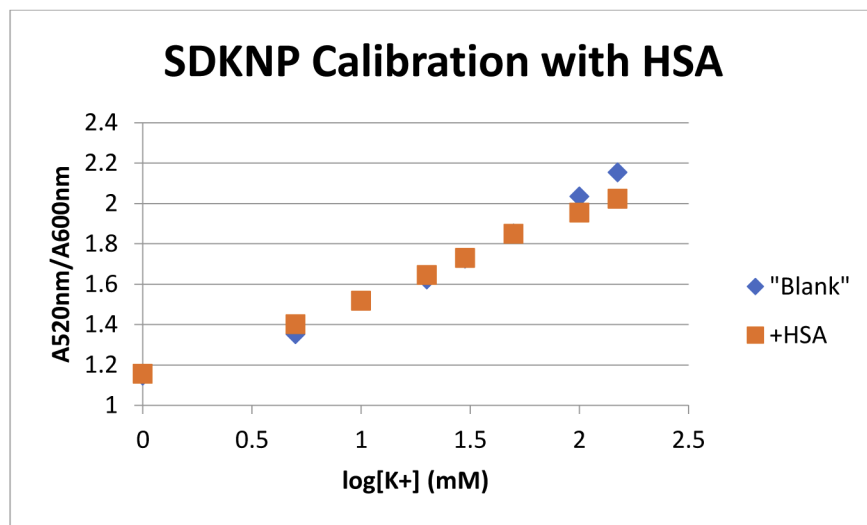

Fig. 10. A comparison of two calibration curves taken of the SDKNP, both in MBS, and one containing 5 mg/mL human serum albumin. As the figure shows, HSA has no influence on the SDKNP's function in the biologically relevant concentration ranges (HSA– 5 mg/mL [38]; K^+ 1-50 mM).

Appendix 3: SDKNP toxicity

An MTT assay, using SDKNP at 1 mg/mL, found that the toxicity of the nanosensor increased overtime, though little toxicity was observed in the first two hours (Fig. 11). The increase in toxicity is likely attributable to degradation of the micelle and subsequent release of valinomycin, whose toxic properties are well known.
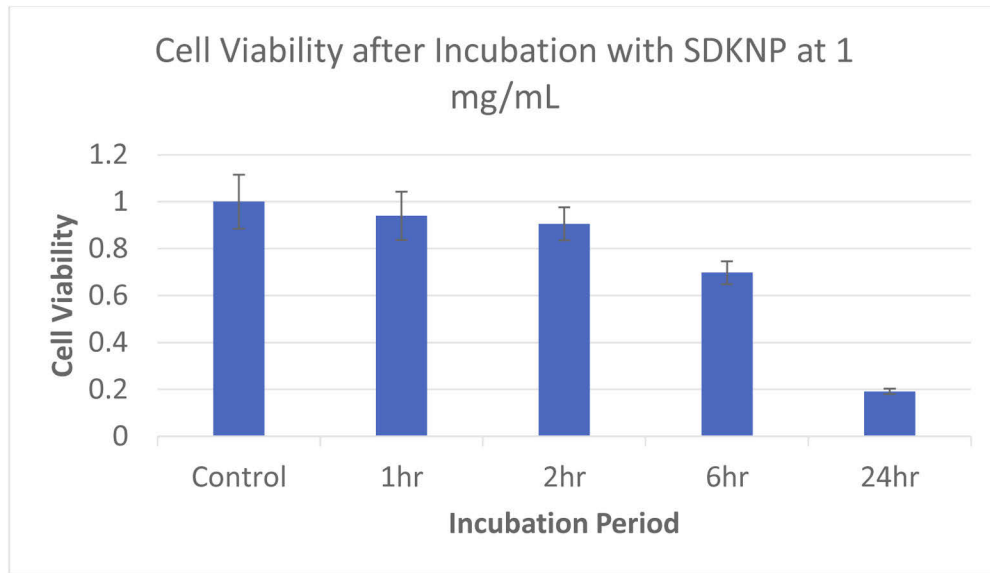
Fig. 11. Results of an MTT assay evaluating the toxicity of the SDKNP. We observe limited toxicity over the first two hours of incubation, but prolonged exposure results in significant cell death. Error bars represent the standard deviation of 4 measurements.

Appendix 4: Photostability of SDKNP

A photostability study of the SDKNP was conducted at a wavelength close to the peak absorption of SDKNP (600 nm). A constant laser energy of 8 mJ/cm^2 was applied for increasing amounts of
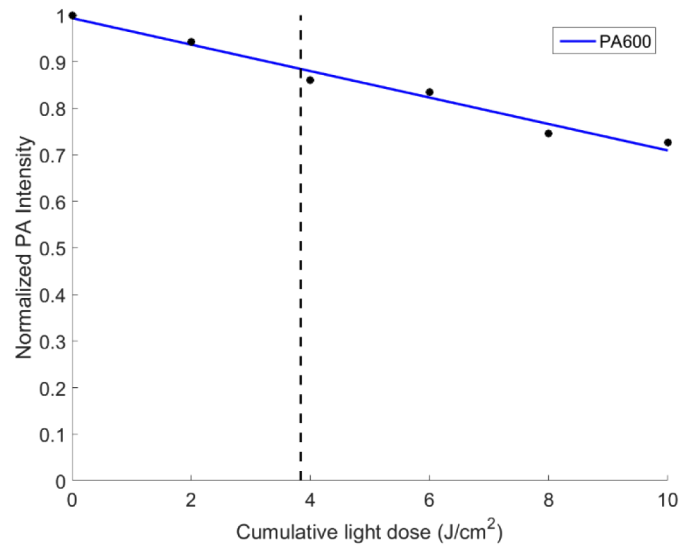
Fig. 12. Results of a photostability study of the SDKNP. The normalized PA intensity of the SDKNP is measured as a function of the cumulative light dose and shows a linear decrease with increasing light dose. The black dotted line indicates the expected cumulative light dose in the *in vivo* imaging (6 wavelengths × 80 images), which corresponds to 88% of the original PA signal at the end of the imaging protocol.

time and the PA signal was measured at various intervals. The PA intensity as a function of the cumulative light dose is shown in Fig. 12. The PA intensity dropped by approximately 12% after being exposed to the cumulative light dose expected in an imaging session.

Funding

Disclosures

The authors declare no conflicts of interest.

References

1. A. Sigel, H. Sigel, and R. K. Sigel, *Interrelations between essential metal ions and human diseases*, 1 ed. (Springer).
2. W. D. Stein, "The Sodium Pump in the Evolution of Animal Cells," Philos. Trans. R. Soc., B **349**(1329), 263–269 (1995).
3. D. V. Dibrova, M. Y. Galperin, E. V. Koonin, and A. Y. Mulkidjanian, "Ancient Systems of Sodium/Potassium Homeostasis as Predecessors of Membrane Bioenergetics," Biochemistry (Moscow) **80**(5), 495–516 (2015).
4. C. D. Bortner, F. M. Hughes, and J. A. Cidlowski, "A Primary Role for K and Na Efflux in the Activation of Apoptosis," J. Biol. Chem. **272**(51), 32436–32442 (1997).
5. I. Mellman, G. Coukos, and G. Dranoff, "Cancer immunotherapy comes of age," Nature **480**(7378), 480–489 (2011).
6. R. Eil, S. K. Vodnala, D. Clever, C. A. Klebanoff, M. Sukumar, J. H. Pan, D. C. Palmer, A. Gros, T. N. Yamamoto, S. J. Patel, G. C. Guittard, Z. Yu, V. Carbonaro, K. Okkenhaug, D. S. Schrump, W. M. Linehan, R. Roychoudhuri, and N. P. Restifo, "Ionic immune suppression within the tumour microenvironment limits T cell effector function," Nature **537**(7621), 539–543 (2016).
7. S. K. Vodnala, R. Eil, R. J. Kishton, M. Sukumar, T. N. Yamamoto, N.-H. Ha, P.-H. Lee, M. Shin, S. J. Patel, Z. Yu, D. C. Palmer, M. J. Kruhlak, X. Liu, J. W. Locasale, J. Huang, R. Roychoudhuri, T. Finkel, C. A. Klebanoff, and N. P. Restifo, "T cell stemness and dysfunction in tumors are triggered by a common mechanism," Science **363**(6434), eaau0135 (2019).
8. I. A. Elabyad, R. Kalayciyan, N. C. Shanbhag, and L. R. Schad, "First In Vivo Potassium-39 (39 K) MRI at 9.4 T Using Conventional Copper Radio Frequency Surface Coil Cooled to 77 K," IEEE Trans. Biomed. Eng. **61**(2), 334–345 (2014).
9. M. Augath, P. Heiler, S. Kirsch, and L. R. Schad, "In vivo 39 K, 23Na and 1H MR imaging using a triple resonant RF coil setup," J. Magn. Reson. **200**(1), 134–136 (2009).
10. R. Umathum, M. B. Rösler, and A. M. Nagel, "In Vivo 39 K MR Imaging of Human Muscle and Brain," Radiology **269**(2), 569–576 (2013).
11. H. Wiig, K. Aukland, and O. Tenstad, "Isolation of interstitial fluid from rat mammary tumors by a centrifugation method," Am J Physiol-Heart C **284**(1), H416–H424 (2003).
12. M. Xu and L. Wang, "Photoacoustic Imaging in Biomedicine," Rev. Sci. Instrum. **77**(4), 041101 (2006).
13. L. V. Wang, "Multiscale photoacoustic microscopy and computed tomography," Nat. Photonics **3**(9), 503–509 (2009).
14. K. J. Cash, C. Li, J. Xia, L. V. Wang, and H. A. Clark, "Optical Drug Monitoring: Photoacoustic Imaging of Nanosensors to Monitor Therapeutic Lithium in Vivo," ACS Nano **9**(2), 1692–1698 (2015).
15. J. Jo, C. H. Lee, J. Folz, J. W. Y. Tan, X. Wang, and R. Kopelman, "In Vivo Photoacoustic Lifetime Based Oxygen Imaging with Tumor Targeted G2 Polyacrylamide Nanosonophores," ACS Nano **13**(12), 14024–14032 (2019).
16. Q. Shao and S. Ashkenazi, "Photoacoustic lifetime imaging for direct *in vivo* tissue oxygen monitoring," J. Biomed. Opt. **20**(3), 036004 (2015).
17. S. Ashkenazi, S. W. Huang, T. Horvath, Y. E. L. Koo, and R. Kopelman, "Oxygen sensing for in vivo imaging by photoacoustic lifetime probing," in 2008), 68560D-68560D-68565.
18. A. Ray, J. R. Rajian, Y.-E. K. Lee, X. Wang, and R. Kopelman, "Lifetime-based photoacoustic oxygen sensing *in vivo*," J. Biomed. Opt. **17**(5), 057004 (2012).
19. Q. Shao, E. Morgounova, C. Jiang, J. Choi, J. Bischof, and S. Ashkenazi, "*In vivo* photoacoustic lifetime imaging of tumor hypoxia in small animals," J. Biomed. Opt. **18**(7), 076019 (2013).
20. J. Jo, C. H. Lee, R. Kopelman, and X. Wang, "In vivo quantitative imaging of tumor pH by nanosonophore assisted multispectral photoacoustic imaging," Nat. Commun. **8**(1), 471 (2017).
21. W. Huang, R. Chen, Y. Peng, F. Duan, Y. Huang, W. Guo, X. Chen, and L. Nie, "In Vivo Quantitative Photoacoustic Diagnosis of Gastric and Intestinal Dysfunctions with a Broad pH-Responsive Sensor," ACS Nano **13**(8), 9561–9570 (2019).
22. C. H. Lee, J. Folz, W. Zhang, J. Jo, J. W. Y. Tan, X. Wang, and R. Kopelman, "Ion-Selective Nanosensor for Photoacoustic and Fluorescence Imaging of Potassium," Anal. Chem. **89**(15), 7943–7949 (2017).
23. X. Xie, I. Szilagyi, J. Zhai, L. Wang, and E. Bakker, "Ion-Selective Optical Nanosensors Based on Solvatochromic Dyes of Different Lipophilicity: From Bulk Partitioning to Interfacial Accumulation," ACS Sens. **1**(5), 516–520 (2016).

24. M. Shortreed, E. Bakker, and R. Kopelman, "Miniature Sodium-Selective Ion-Exchange Optode with Fluorescent pH Chromoionophores and Tunable Dynamic Range," Anal. Chem. **68**(15), 2656–2662 (1996).

25. S. L. R. Barker, B. A. Thorsrud, and R. Kopelman, "Nitrite- and Chloride-Selective Fluorescent Nano-Optodes and in Vitro Application to Rat Conceptuses," Anal. Chem. **70**(1), 100–104 (1998).

26. M. G. Brasuel, T. J. Miller, R. Kopelman, and M. A. Philbert, "Liquid polymer nano-PEBBLEs for Cl- analysis and biological applications," Analyst **128**(10), 1262–1267 (2003).

27. Q. Yu, S. Huang, Z. Wu, J. Zheng, X. Chen, and L. Nie, "Label-free Visualization of Early Cancer Hepatic Micrometastasis and Intraoperative Image-guided Surgery by Photoacoustic Imaging," *J. Nucl. Med.* (2019).

28. S. Kim, Y.-S. Chen, G. P. Luke, and S. Y. Emelianov, "In vivo three-dimensional spectroscopic photoacoustic imaging for monitoring nanoparticle delivery," Biomed. Opt. Express **2**(9), 2540–2550 (2011).

29. E. Merčep, X. L. Deán-Ben, and D. Razansky, "Imaging of blood flow and oxygen state with a multi-segment optoacoustic ultrasound array," Photoacoustics **10**, 48–53 (2018).

30. M. U. Arabul, M. C. M. Rutten, P. Bruneval, M. R. H. M. van Sambeek, F. N. van de Vosse, and R. G. P. Lopata, "Unmixing multi-spectral photoacoustic sources in human carotid plaques using non-negative independent component analysis," Photoacoustics **15**, 100140 (2019).

31. G. P. Luke, S. Y. Nam, and S. Y. Emelianov, "Optical wavelength selection for improved spectroscopic photoacoustic imaging," Photoacoustics **1**(2), 36–42 (2013).

32. L. J. Steven, "Optical properties of biological tissues: a review," Phys. Med. Biol. **58**(11), R37–R61 (2013).

33. K. Maslov, H. F. Zhang, and L. V. Wang, "Effects of wavelength-dependent fluence attenuation on the noninvasive photoacoustic imaging of hemoglobin oxygen saturation in subcutaneous vasculaturein vivo," Inverse Probl. **23**(6), S113–S122 (2007).

34. A. Bauer, R. Nothdurft, J. Culver, T. Erpelding, and L. Wang, "Quantitative photoacoustic imaging: correcting for heterogeneous light fluence distributions using diffuse optical tomography," J. Biomed. Opt. **16**(9), 096016 (2011).

35. K. Daoudi, A. Hussain, E. Hondebrink, and W. Steenbergen, "Correcting photoacoustic signals for fluence variations using acousto-optic modulation," Opt. Express **20**(13), 14117–14129 (2012).

36. E. M. Y. E. Koo Lee, M. Brasuel, M. Philbert, and R. Kopelman, "PEBBLE Nanosensors for In Vitro Bioanalysis," in *CRC Biomedical Photonics Handbook*, 2nd ed., T. Vo-Dinh, ed. (CRC Press, Boca Raton, 2014), p. 767.

37. A. Pitto-Barry and N. P. E. Barry, "Pluronic® block-copolymers in medicine: from chemical and biological versatility to rationalisation and clinical advances," Polym. Chem. **5**(10), 3291–3297 (2014).

38. M. Kroll, "*Tietz Textbook of Clinical Chemistry*, 3 Edition. Carl A. Burtis and Edward R. Ashwood, eds. WB Saunders, Philadelphia, PA 1998, 1917 pp., $195.00. ISBN 0-7216-5610-2," Clinical Chemistry 45, 913-914 (1999).